Medical & Biological Engineering & Computing
https://doi.org/10.1007/s11517-017-1755-2

ORIGINAL ARTICLE

Multimodal molecular 3D imaging for the tumoral volumetric distribution assessment of folate-based biosensors

Gerardo J. Ramírez-Nava [1,2] · Clara L. Santos-Cuevas [1] · Isaac Chairez [3] · Liliana Aranda-Lara [1,2]

Received: 27 June 2016 / Accepted: 20 November 2017

Abstract
The aim of this study was to characterize the in vivo volumetric distribution of three folate-based biosensors by different imaging modalities (X-ray, fluorescence, Cerenkov luminescence, and radioisotopic imaging) through the development of a tridimensional image reconstruction algorithm. The preclinical and multimodal Xtreme imaging system, with a Multimodal Animal Rotation System (MARS), was used to acquire bidimensional images, which were processed to obtain the tridimensional reconstruction. Images of mice at different times (biosensor distribution) were simultaneously obtained from the four imaging modalities. The filtered back projection and inverse Radon transformation were used as main image-processing techniques. The algorithm developed in Matlab was able to calculate the volumetric profiles of ^{99m}Tc-Folate-Bombesin (radioisotopic image), ^{177}Lu-Folate-Bombesin (Cerenkov image), and FolateRSense™ 680 (fluorescence image) in tumors and kidneys of mice, and no significant differences were detected in the volumetric quantifications among measurement techniques. The imaging tridimensional reconstruction algorithm can be easily extrapolated to different 2D acquisition-type images. This characteristic flexibility of the algorithm developed in this study is a remarkable advantage in comparison to similar reconstruction methods.

Keywords Tridimensional reconstruction · Inverse Radon transformation · In vivo imaging · Folate-based biosensors

1 Introduction

Molecular imaging of living subjects is an emerging field that aims to study molecular and cellular events in the intact living animal and human [1]. The information in this field is obtained by biosensors which are designed to target specific biological sites [2, 3]. The biosensors emit a signal that can be captured by a suitable image acquisition system because they are usually labeled with fluorescent molecules [4–6], radionuclides such as gamma [7, 8] or positron emitters [6, 9], etc. [10, 11].

The heterobivalent radioconjugate ^{99m}Tc-Folate-Bombesin and the ^{177}Lu-Folate-Bombesin theranostic radiopharmaceutical have been reported as biosensors for application in medical diagnosis and radiotherapy of breast cancer due to the concomitant recognition of folate receptor α (FRα) and gastrin-releasing peptide receptor (GRPr) [7, 12]. FRα and GRPr have been reported as receptors overexpressed in breast cancer [13–17].Thus, these receptors can be used as good imaging targets for volumetric characterization in breast tumors.

An imaging trend that has been intensified in recent years is the development and commercialization of different multimodal imaging systems (MIS) [18, 19]. MIS have emerged as devices with an operation strategy that combines the strengths of different imaging modalities and produces a hybrid platform with superior capacities to those of its individual components [20]. One area that has been supported by using dedicated MIS is preclinical in vivo small animal imaging to obtain complementary

✉ Clara L. Santos-Cuevas
clara_letici@yahoo.com.mx

Gerardo J. Ramírez-Nava
gerjul5420@hotmail.com

Isaac Chairez
isaac_chairez@yahoo.com

Liliana Aranda-Lara
lilyar27@yahoo.com.mx

[1] Instituto Nacional de Investigaciones Nucleares (ININ), 52750 Ocoyoacac, Estado de México, Mexico

[2] Facultad de Medicina, Universidad Autónoma del Estado de México, 50180 Toluca, Estado de México, Mexico

[3] Unidad Profesional Interdisciplinaria de Biotecnología (UPIBI), Instituto Politécnico Nacional (IPN), Gustavo A. Madero, 07340 Mexico City, Mexico

Published online: 01 December 2017

information of several metabolic diseases with both functional and anatomical details [21–23].

An example of this equipment is Bruker's In-Vivo Xtreme (BVX) [11, 19, 24]. BVX is a preclinical multimodal imaging system which acquires images through four different modalities: radiographic, radioisotopic, fluorescence, and luminescence [18]. BVX relies on optical technology to get radiopharmaceutical imaging. Unlike conventional nuclear imaging systems (SPECT), BVX has an ultra-thin phosphor screen that functions as a scintillator device, a charge couple device detector, and lacks a pulse height analyzer for discriminating the different energies emitted by the radionuclide [25]. Also, BVX has a Multimodal Animal Rotation System (MARS), which is designed to capture images on a coverage range of 360° [19, 26], but it does not have an automatic volumetric reconstruction system. Despite this disadvantage, computational algorithms can be used to obtain 3D reconstructions from an ordered sequence of projected 2D images at different angles like those acquired by the BVX/MARS.

Three-dimensional reconstruction includes the application of filtered back projection [20, 27, 28], iterative [29–31], and analytic [32] image-processing methods. Among these methods are the modified FDK algorithm (a modified back projection method) for computerized tomography volume reconstruction, algebraic reconstruction technique, and the Radon transform algorithm based on fluorescence reconstruction [33–35]. The 3D surface reconstruction method based on the back projection method using white/black images [27] can be considered a relevant example of 3D imaging procedures. Other authors propose a reconstruction procedure using a modality fusion approach of bioluminescent sources from optical data, measured on the body surface of mice. Another reconstruction method for bioluminescence tomography has been proposed based on establishing a relationship between measured surface photon density and an unknown bioluminescence source distribution. A finite element method that considers the diffusion approximation of photon propagation in biological tissue is the theoretical basis of this method.

The filtered back projection method is based on simple back projection, which usually blurs the image traits, but includes a previous filtering or kernel convolution of each frame [36, 37]. This filter in the spatial domain is represented by:

$$p'(x) = p(x) \otimes k(x) \tag{1}$$

where $p(x)$ is the original projection data, $k(x)$ is the kernel, $p'(x)$ is the resultant filtered data, and $\otimes$ represents the integral convolution operation.

Equation 1 is represented in the frequency domain and is known as Fourier slice theorem. Thus, the following representation is valid:

$$p'(x) = FT^{-1}(FT(p(x)) * K(f)) \tag{2}$$

where $K(f)$ is the Fourier transform of the kernel. Despite of the fact that many kinds of kernels that can be used depending on the imaging application exist, the most efficient for clinical images are Shepp-Logan, cosine, or Hamming filters that compensate high-frequency roll-off [38].

The aim of this study was to develop an algorithm based on filtered back projection of 2D projected images acquired by the BVX/MARS. The reconstructed images were used to evaluate the in vivo volumetric distribution of different folate biosensors. In particular, the reconstruction method was applied to measuring kidney and tumor uptake of folate. The cross correlation of X-ray, fluorescence, Cerenkov luminescence, and radioisotopic imaging acquired using the BVX/MARS yields to characterize the efficiency of folate as an in vivo biosensor.

2 Material and methods

2.1 Animal model

The animals used in this study were nu/nu athymic mice with weights between 20 and 24 g. The mice were obtained from "Instituto Nacional de Ciencias Médicas y Nutrición Salvador Zubirán." They were kept in sterile cages with beds of sterile wood shavings, constant temperature, humidity, noise, and 12:12 light periods. Water and feed (standard PMI 5001 feed) were given ad libitum. Tumors were induced by subcutaneous injection of T47D breast cancer cells into the back of the athymic nude mice. Tumor induction and biodistribution studies in mice were carried out according to the rules and regulations of the Official Mexican Norm 062-ZOO-1999. Biological wastes were managed and disposed according to the Official Mexican Norm -087-ECOL-SSA1-2002. The study was approved by the Institutional Ethical Committee for the Care and Use of Laboratory Animals ("Instituto Nacional de Ciencias Médicas y Nutrición Salvador Zubirán").

2.2 Biosensors

In order to obtain and evaluate the biosensors uptake, fluorescence, Cerenkov luminescence, and radioisotopic modalities were used. Three different folate-based biosensors were applied and each one of them was detected by a different imaging modality of the BVX system [18].

The fluorescence images were acquired with the Perkin Elmer®'s FolateRSense™680, which is a near-infrared fluorescent folate-targeted agent that can be used to image folate receptor expression in tumors [6].

For Cerenkov luminescence images, the ^{177}Lu-Folate-Bombesin [(Lys^{1}(folic acid)Lys^{3}(^{177}Lu-DOTA)-Bombesin(1-14))] biosensor was prepared as previously reported [7]. This

radiopharmaceutical is labeled with ^{177}Lutetium, which is a β^- particle-emitting radionuclide with a physical half-life of 162 h (6.73 days) and its β^- particles have a maximum energy of 498 keV and a mean energy of 133 keV, which is sufficient to produce the Cerenkov effect (threshold beta particle energy to produce Cerenkov effect in tissue is between 213 and 260 keV) [12].

For radioisotopic images, the ^{99m}Tc-Folate-Bombesin [(Lys^1-(folic acid)-Lys^3(^{99m}Tc-EDDA/HYNIC)-Bombesin(1-14))] biosensor was prepared as previously reported. ^{99m}Tc is an ideal agent for diagnostic imaging because of its physical half-life, ease in compounding and relatively low dose to the patient. The ^{99m}Tc gamma emission of 140 keV allows acquisition of radioisotopic images [7, 8].

2.3 Animal preparation

The mice were anesthetized to minimize their movement during image acquisitions. The animals were placed individually in an induction chamber, and anesthesia was induced with 2% isoflurane in 100% oxygen. In order to achieve a contrast enhancement which would facilitate the visualization and outline of certain body parts such as kidneys and bladder, the iodinated contrast agent Xenetix® 300 was injected into the mouse tail vein 30 min before X-ray imaging [39]. Then, all mice were placed in the same position within the BVX/MARS chamber to preserve the spatial alignment between the image acquisitions.

2.4 Image acquisition

All the optical images were acquired with the BVX (Fig. 1a). After biosensor injection, the mice were rotated with the MARS (Fig. 1b). BVX software allows individual or multiple acquisitions. The former case is done directly through the acquisition menu. In the case of multiple acquisitions, it is necessary to set a protocol which strings the acquisition settings together in order to automatically capture a series of images as part of the experiment. In both cases (individual or multiple acquisitions), parameters such as binning, exposure time, field of view (FOV), and accumulation path had to be specified.

The X-ray parameters were energy of 45 kVp, current of 497 μA, and an aluminum filter of 0.8 mm. The exposure time was 10 s, a 1 × 1 binning, 12.5 cm FOV, and 0–360° coverage with 2° steps. Radioisotopic images were acquired by an ultrathin and uniform radioisotopic phosphor screen, with an exposure time of 3 min, a binning of 4 × 4, a FOV of 12.5 cm, and 20° steps. A parallel-hole collimator was used to reduce the effect of scattered radiation. Fluorescence images were acquired with an exposure time of 2 s; the binning was 4 × 4, a FOV of 12.5 cm, and 15° steps. FolateRSense™ 680 excitation and emission wavelengths were 690 and 750 nm, respectively. In the case of Cerenkov luminescence images, the exposure time was 5 min, the binning was 4 × 4, a FOV of 12.5 cm, and 30° steps.

2.5 Tridimensional reconstruction algorithm

An algorithm based on the inverse Radon transform and the filtered back projection was implemented on a set of planar images acquired by the BVX at different rotation angles. The angle resolution was modified according to the acquisition period. This strategy follows the regular tomographic methodology to obtain tridimensional reconstructions of biosensors uptake. The computational algorithm was programmed in Matlab® R2013a and was executed in a DELL ALIENWARE15 with an Intel 2.60 GHz Core i-7, 16 GB of RAM and a Windows 8 operating system. The algorithm took around 5 min to obtain the reconstructed object. The reconstruction algorithm is divided in two stages: the image adequation (Fig. 2) and the obtention of the 3D reconstructed object (Fig. 3). The steps of each stage are described below:

2.5.1 Image adequation

Image exportation The images of the different modalities are acquired through an acquisition protocol and are then saved in BIP files. Considering that BIP is not a supported image format in Matlab, images were exported into DICOM files (Fig. 2a).

Image reading and resizing Once the image files were in DICOM format, a reading procedure extracted the images from the DICOM files and represented them in the workspace as bidimensional arrays of class uint16. X-ray images were 1024 × 1024 pixels; while radioisotopic, fluorescence, and Cerenkov luminescence images were 512 × 512 pixels. As the images had to be of the same size, the X-ray images were reduced to the 512 × 512 pixel size using a rescaling process (Fig. 2b).

Image cropping Considering that the images had pixels that do not provide useful information, they were cropped, mainly leaving the pixels that represented an organ, a structure or the biosensors uptake. This was achieved through a spatial transformation that cut certain regular regions in the image (Fig. 2c). This cropping was applied in all the images in order to decrease the computational cost of the algorithm. This process was automatically executed over the entire set of images, giving as result images of 512 × 211 pixels (Fig. 2d).

Interpolation algorithm With the images acquired by the BVX, a 3D matrix of the original grayscale images was structured (Fig. 2e). Image acquisition in different modalities, at all the angles (0–360° with 1° steps), is not viable because of the internal BVX processing time. Therefore, we considered to take as many images as possible in each particular modality. Then, an algorithm to obtain interpolated images was developed. This algorithm took pixel by pixel of the two original

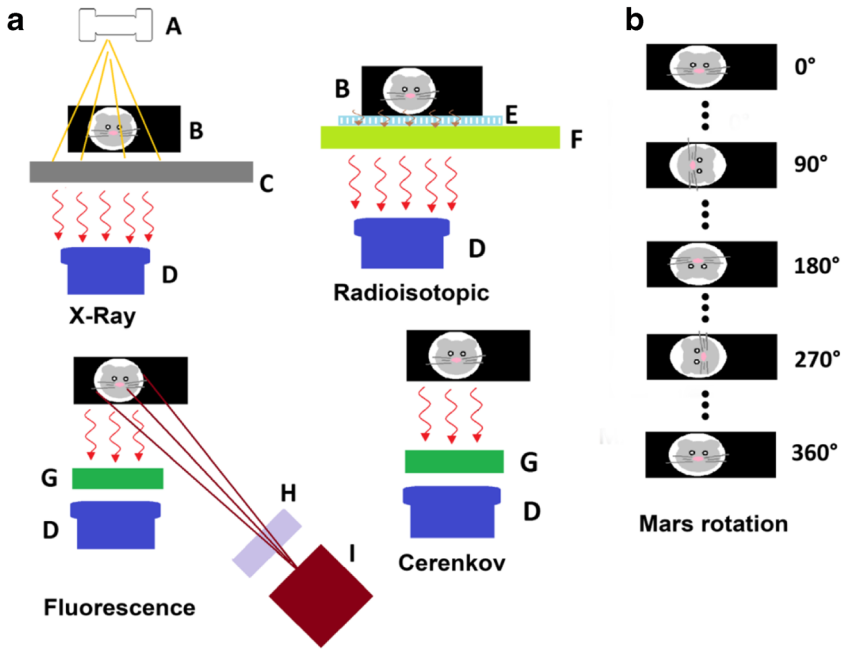

Fig. 1 **a** BVX elements by which images of the 4 different modalities were acquired: A. X-ray tube; B. MARS; C. X-ray phosphor screen; D. CCD camera; E. parallel-hole collimator; F. radioisotopic phosphor screen; G. emission filters; H. excitation filters; I. xenon lamp. **b** Example of a 90° step rotation of MARS

images and made an interpolation in order to acquire new images and pixel values. This process was executed on every pixel of each row and column. A series of interpolated images corresponding to the missing angles were acquired and a new array, which contained original and the interpolated images, was designed (Fig. 2f).

Image processing/characterization of pixel values Depending on the imaging modality used to obtain the 3D reconstructed image, pixel intensity values of skeleton, tumors, kidneys, and biosensors uptake were characterized to discern between them at the time of reconstruction (Fig. 2g). In the specific case of X-ray images, there was an extra step, the X-ray MARS chamber subtraction. For this purpose, X-ray images of the empty MARS chamber at different angles were acquired. Then, these images were subtracted from the mouse X-ray images that were taken previously, leaving only the anatomical information of mice.

The pixel characterization of different tissues and biosensors uptake is described below:

- Skeleton: So as to get bone enhancement in the X-ray images, a pre-adjust of image intensity values was done using a contrast adjustment procedure [40, 41]. The contrast of the output images was increased by at least 88.06%. Then, a sharpening process was applied to each image, yielding an enhanced version of the grayscale of the input image. In consequence, image features such as edges were sharpened using an unsharp masking method

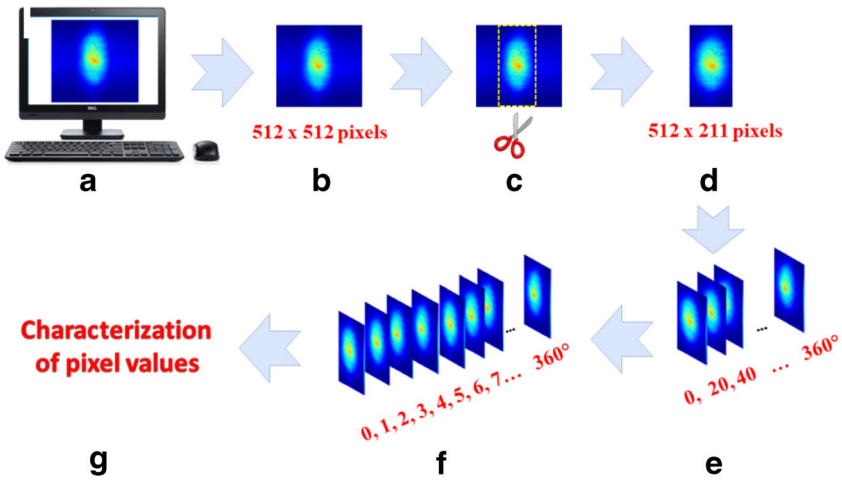

Fig. 2 Image adequation flowchart. a) Image exportation; b) Image reading and resizing; c) Image cropping; d) Image cropped; e) Interpolation algorithm input; f) Interpolation algorithm output; g) Image processing/characterization of pixel values

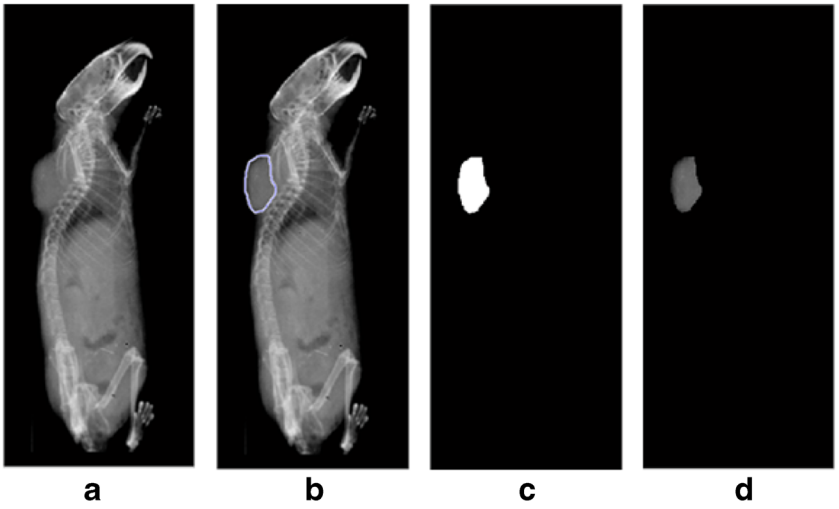

Fig. 3 **a** Original X-ray image. **b** Freehand drawing of the mask corresponding to tumors. **c** Binary mask obtained from the drawing of the ROI. **d** Result of the masking process of tumoral tissue

[42, 43]. After that, an automatic binary mask was created to recover the region of interest in the acquired image. These binary masks were overlapped to the X-ray images leaving only the mice skeleton.

- Tumors: Due to the variability of tumor morphology, regions of interests (ROIs) were not calculated automatically. For this purpose, binary masks were drawn manually using the free-hand drawing process. Then, these binary masks were overlapped to the X-ray images leaving only the tumor areas. This process was repeated on each image (Fig. 3).
- Kidneys: Considering their spatial location and the surrounding tissues, an automatic binary mask was created. The binary masks were overlapped to the X-ray images, leaving only the kidney area.
- Biosensors uptake/activity: Preliminary image intensity adjustment was done. Then, a morphological opening on the grayscale was performed. After, an automatic binary mask was created that was overlapped to the fluorescence, Cerenkov luminescence, and radioisotopic image, leaving only the biosensors uptake regions.

2.5.2 Obtention of the 3D reconstructed object

Reconstruction matrix From the whole set of individual processed images $I_0 \in \mathbb{R}^{m \times n}$ (experimental and interpolated) (Fig. 4a), the algorithm took the same row of each image $I_{0,\,i} \in \mathbb{R}^m$ (Fig. 4a, R1, I (0°), R1, I (90°)… R1, I (360°)). These rows served to construct an auxiliary matrix $I_1 \in \mathbb{R}^{360 \times n}$ (Fig. 4b). The corresponding matrix I_1 is transposed to generate $I_2 \in \mathbb{R}^{n \times 360}$. Each matrix I_2 has the same number of columns in every angle corresponding to the row. This process was repeated for each row in all the images giving as result a new array of m matrices (Fig. 4c). For each matrix obtained in the previous step, the inverse Radon transform was applied by implementing the filtered back projection (Fig. 4d). The filtered back projection is the most widely used reconstruction algorithm in commercial equipment and consists in the filtering of measured projections data at different projection angles with a special function and the back projection of the filtered projection data to get the reconstructed object. In the case of the Matlab function, the filter is designed in the frequency domain and then multiplied by the fast Fourier transform (FFT) of the projections. To avoid the spatial domain aliasing, the projections are zero-padded to a power of 2 before filtering.

As a result of the filtered back projection, axial slices of the tridimensional volume to be reconstructed were obtained (Fig. 4e). Each axial slice was stacked, resulting in the final reconstruction array (Fig. 4f).

Deployment/visualization The reconstructed volume was obtained with an isosurface (Fig. 4g). If we have a function defined over $f(x, y, z)$, then we can select all the elements whose values are less or equal than a predefined value (isovalue). This set of elements can be identified in each slice. As result, a so-called isosurface function (X, Y, Z, V) is obtained, which determines the contour from volume data "V" given by the isovalue. The arrays in X, Y, and Z define the coordinates for the volume. The output from this function is the faces and vertices corresponding to the isosurface used for displaying the region of interest in the 3D domain [44].

2.6 Tridimensional fusion between modalities

The tridimensional fusion was achieved using the superposition of the values obtained in the reconstruction matrices and modifying the transparency of each image. This parameter is specific to each graphic (the image acquired in a different modality) object and can assume values between 0 and 1, where "0" represents full transparency of the object and "1" represents full intensity.

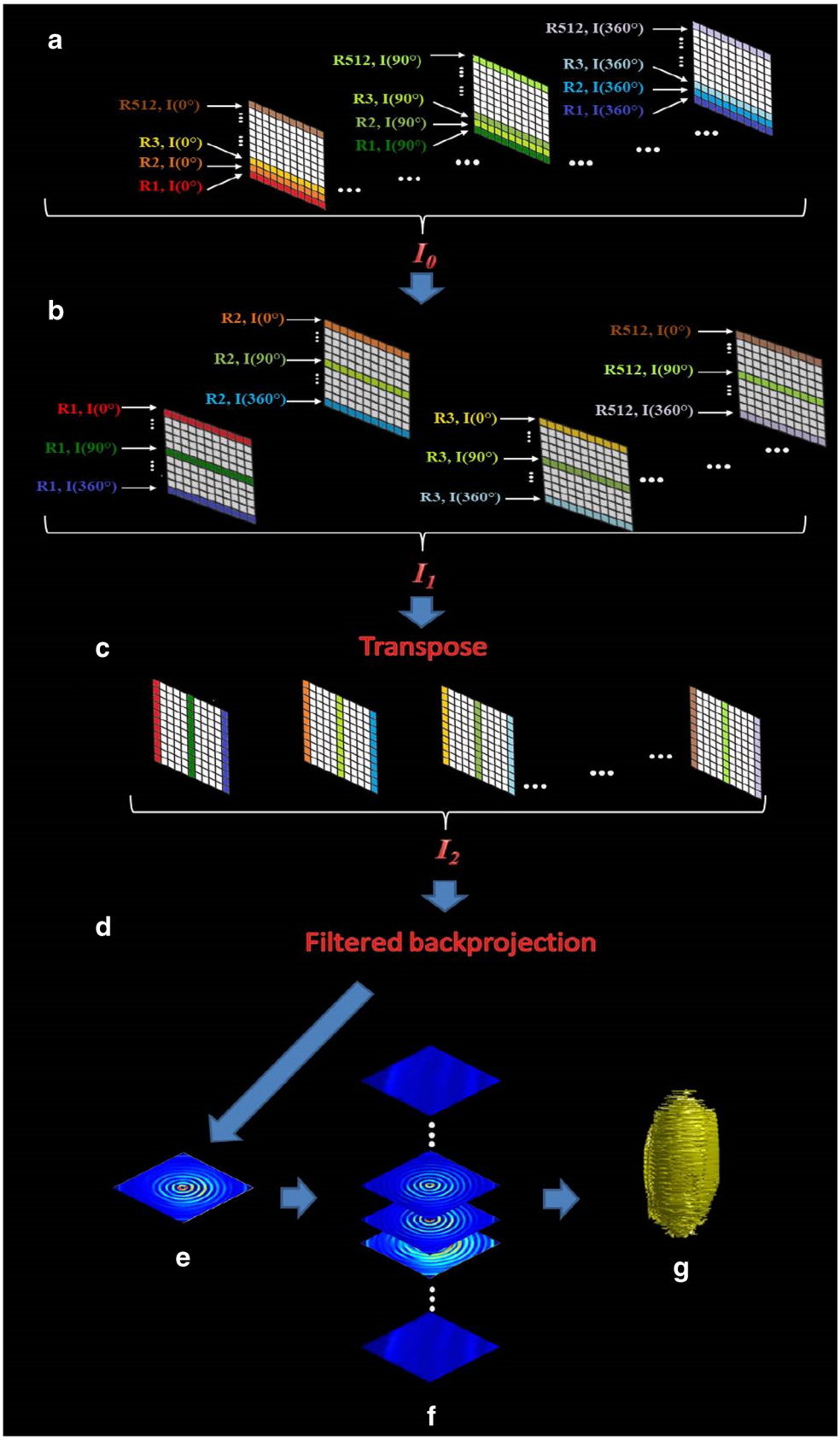

Fig. 4 Flowchart for the obtention of the 3D reconstructed object a) Set of individual processed images; b) Auxiliary matrix I_1; c) Transposed matrix I_2; d) Filtered back projection; e) Axial single slice; f) Stack of axial slices; g) 3D isosurface visualization

2.7 Volumetric quantification

The volume calculation was done via surface detection. This consisted in the identification of all the voxels which were contained in the reconstructed object of interest and then multiplication of the number of said voxels by the voxel volume. The dimensions of each voxel were 0.181 mm × 0.181 mm × 0.201 mm. The approximate volume of the tumors was calculated using the ellipsoid volume formulas pi/6 × L × W × H and ½ × L × W × H, where "L" is the length, "H" is the height, and "W" is the width [45]. The results of these calculations were compared with the volumes obtained in the tridimensional reconstruction algorithm.

2.8 Tumor and kidney uptake percentage

The uptake percentage of tumors and kidneys was calculated dividing the volume of the biosensor uptake by the total volumes of the structure under analysis. The uptake percentage of the three biosensors at different times was calculated for each image modality using Eq. 3.

$$\%\mathrm{OBU} = \frac{Volume\ of\ biosensor\ in\ the\ organ\ of\ interest}{Volume\ of\ the\ organ\ of\ interest} * 100 \tag{3}$$

2.9 Activity quantification

Attenuation factor calculation To calculate the BVX attenuation factor (AF) due to mice thicknesses in radioisotopic images, a set of four known ^{99m}Tc radiation activity (1.73 ± 0.09, 3.89 ± 0.19, 8.03 ± 0.46, 11.09 ± 0.72 MBq/200 μl) samples ($n = 3$) were placed inside the MARS chamber in two different geometry groups. The first experiment positioned a mouse between the MARS chamber and the imaging system sensor (Fig. 5a). The second one used the same known samples, but for this particular case, no mouse was placed inside the MARS chamber (Fig. 5b). The radiation activity of each sample (with and without mouse) at 0°, 90°,180°,270°, and 360° was quantified by a computer software. The AF was calculated as the quotient of the total intensity without the mouse (IWOM), divided by the total intensity including the mouse (IWM).

$$AF = \frac{Total\ intensity\ without\ the\ mouse}{Total\ intensity\ with\ the\ mouse} = \frac{IWOM}{IWM} \tag{4}$$

Evaluation of scattering To calculate the scattering and calibration factors, nine different known ^{99m}Tc radiation activities (Fig. 6, images A1, B1, C1, D1, E1, F1, G1, H1, and I1, with activity concentrations of 14.99 ± 0.01, 25.98 ± 0.02, 55.91 ± 0.07, 104.63 ± 0.30, 139.07 ± 0.73, 184.36 ± 1.29, 222.37 ± 2.07, 290.86 ± 3.26, and 350.46 ± 5.13 MBq/200 μl, respectively, were placed in 0.6 mL tubes of 0.6 ml. Using the BVX, a set of images was acquired from each tube ($n = 5$).

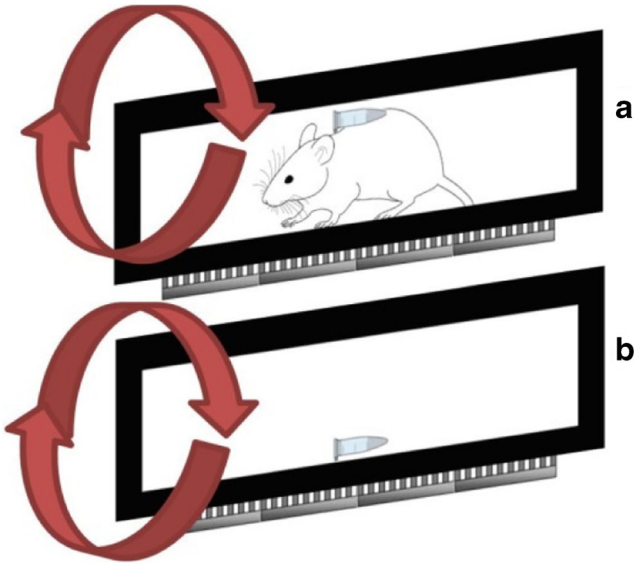

Fig. 5 Lateral view of the general scheme used in the acquisition and calculation of the attenuation factor

Radioisotopic images were cropped, leaving only the pixels that have both primary and scattered radiation (Itot) (Fig. 7a). The area of the tube which contained the primary radiation in pixels was calculated with the information from an X-ray image (Ia) (Fig. 7b). Using this data, the mask 1 (M1) was obtained (Fig. 7c). Mask 2 (M2) was calculated as the complement of M1 (Fig. 7d). The set of these two masks (M1 and M2) and an example showing how they were applied on unprocessed image *Itot* are shown in Fig. 7. *Iact* (Fig. 7e) was obtained by the direct

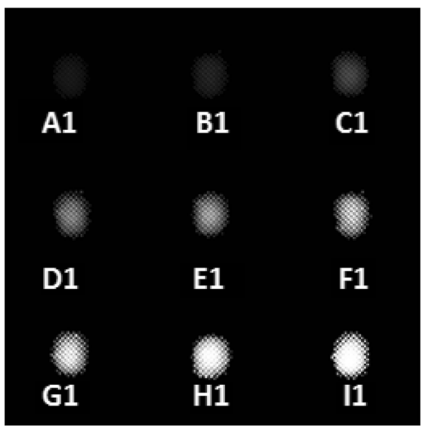

Fig. 6 ^{99m}Tc radiation activities used in the calculation of the scattering factor

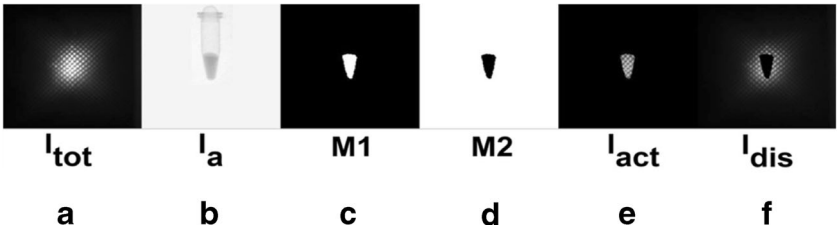

Fig. 7 Image processing for the scattering factor calculation

multiplication (pixel by pixel) of Itot and M1. A similar procedure was followed to obtain the image *Idis* (Fig. 7f), which corresponds to the application of M2 over *Itot*. Normalized intensity (intensity/pixel) in each image was calculated. Total intensity per pixel of the total image (INt), the normalized intensity due to the activity in the tube (INa), and the normalized intensity due to scattering (INd) were also determined. From the collected information, the relation of [INt vs. (INt-INd)] was analyzed. For this relation, a function was fitted to obtain the scattering factor.

Calibration factor After being corrected by the attenuation and scattering factors, the planar images of the nine tubes acquired by the BVX were used in the 3D reconstruction algorithm. The mean voxel value was obtained from each reconstruction; from this data, the voxel's grayscale-value characterization curve was obtained. The gray scale mean value of voxel activities was used to quantify the tumor and kidney activity based on image-processing methods.

2.10 Statistical analysis

Comparisons in the tumor volumetric quantification among methods (analytical measurements vs. reconstruction algorithm) were made through an analysis of variance (ANOVA) to detect significant changes. Statistical significance was set at $p < 0.05$. The same analysis was carried out when data of volumetric uptake percentage among mice with the same biosensor was compared.

3 Results

3.1 Images acquired

Images of the four different modalities were acquired with the BVX/MARS. The X-ray protocol was designed to acquire 181 images, while fluorescence, Cerenkov luminescence, and radioisotopic protocols considered the acquisition of 25, 13, and 19 images, respectively. Figure 8 depicts the images of three different mice and the biosensors uptake visualized in each imaging modality. The X-ray images (Fig. 8a–e) give visual information about the tumor localization and the other imaging modalities (Fig. 8a–e) confirm the presence of tumoral tissue.

3.2 Tridimensional reconstruction

In vivo imaging results showed that the proposed reconstruction algorithm allows the obtention of representative anatomic 3D views (X-ray imaging). The radioisotopic, fluorescence, and Cerenkov imaging methods showed a reliable tumor and kidney

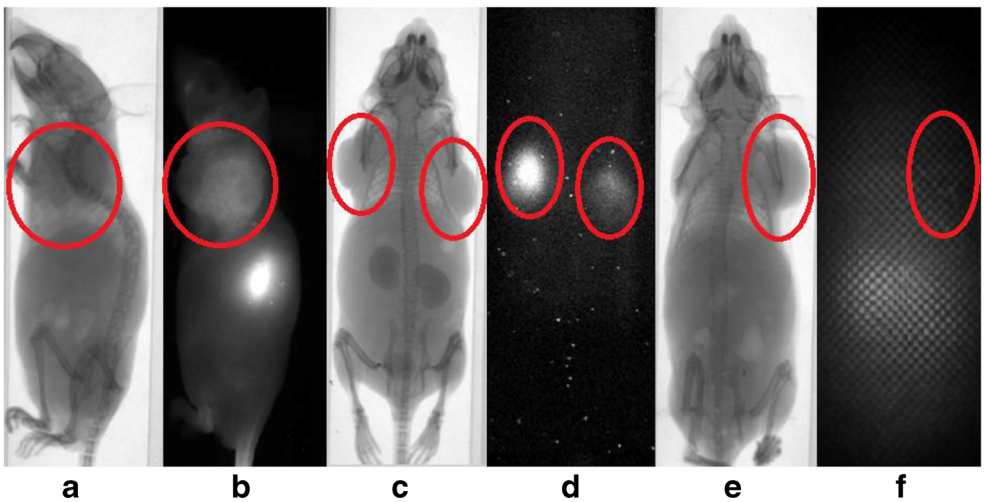

Fig. 8 Examples of 2D projections of different modalities. **a**, **c**, **e**. X-ray images. **b** Fluorescence image. **d** Cerenkov luminescence image. **f** Radioisotopic image. Red circles show tumor localization

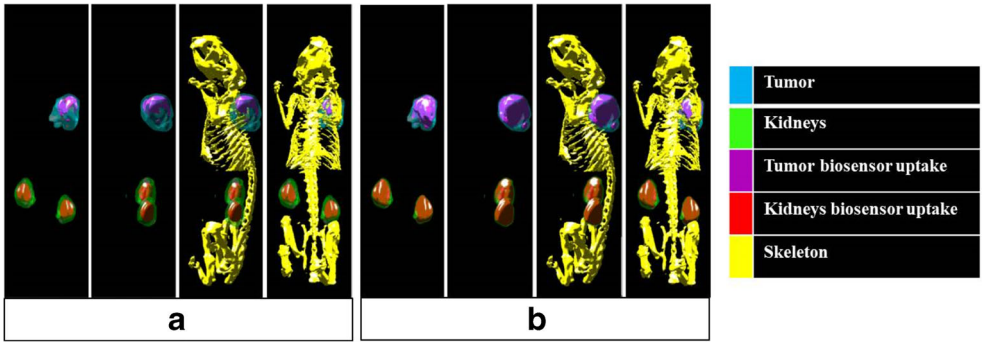

Fig. 9 Tridimensional fusion of mouse skeleton (yellow), kidneys (green), and tumor (cyan). **a** FolateRSense ™ 680 uptake at 6 h. **b** FolateRSense ™ 680 uptake at 24 h

reconstruction. The fusion algorithm results are shown in Fig. 9. The fusion images displayed an accurate anatomic correspondence (in regards to the X-ray image localization) between the uptake regions of interest and the skeleton reconstruction.

3.3 Tumor volumetric quantification and volumetric uptake

Table 1 shows the results of the tumor volumetric quantification by three methods for nine different mice, the tumor and kidney volumetric uptake percentages for the three biosensors quantified at two different times (0.5 and 24 h for radioisotopic, 1 and 24 h for Cerenkov, 6 and 24 h for fluorescence). The statistical analysis between results with two reported methods of tumor volumetric quantification vs. the algorithm proposed in this study did not show statistical difference. These three methods were evaluated over different tumor sizes, and no variances were determined. This seems to be a feasible manner to validate the algorithm designed in this study. The percentage of tumor and kidney uptake values with the three biosensors at two different times show correspondence between mice of the same group (no statistical difference). The comparison between biosensors did not apply because the acquisition times were not the same. However, since the probe is similar, in that, the three biosensors have folic acid in their structure, and the comparative biodistribution showed similar uptakes in the same organs.

Table 1 Tumor volume quantification by three different methods and percentage of volumetric uptake of the three biosensors (mean ± SD)

Biosensors	Mouse	Time (h)	Tumor volumetric quantification			% Volumetric uptake	
			ATV1 (cm^3)	ATV2 (cm^3)	CTV (cm^3)	% VTU	% VKU
^{99m}Tc-Folate-Bombesin	1	0.5	2.38 ± 0.13	2.27 ± 0.12	2.18 ± 0.11	97.04 ± 2.12	90.21 ± 0.81
		24	3.05 ± 0.25	2.92 ± 0.14	2.80 ± 0.13	18.63 ± 1.39	73.35 + 0.24
	2	0.5	0.88 ± 0.08	0.84 ± 0.06	0.85 ± 0.05	98.07 ± 1.75	90.94 ± 0.30
		24	1.06 ± 0.08	1.01 ± 0.08	1.02 ± 0.06	16.79 ± 1.50	71.77 ± 0.66
	3	0.5	2.30 ± 0.15	2.19 ± 0.13	2.15 ± 0.12	98.06 ± 1.88	86.58 ± 0.14
		24	2.82 ± 0.23	2.69 ± 0.31	2.64 ± 0.24	14.00 ± 1.58	68.05 ± 0.11
FolateRSense ™ 680	4	6	1.69 ± 0.16	1.61 ± 0.11	1.62 ± 0.12	23.69 ± 1.92	47.16 ± 0.93
		24	2.84 ± 0.15	2.71 ± 0.17	2.86 ± 0.19	60.06 ± 1.98	96.01 ± 1.44
	5	6	1.48 ± 0.11	1.41 ± 0.12	1.51 ± 0.1	25.18 ± 0.88	41.01 ± 2.91
		24	2.15 ± 0.17	2.06 ± 0.12	2.03 ± 0.13	52.71 ± 0.71	94.19 ± 1.33
	6	6	0.67 ± 0.02	0.64 ± 0.04	0.69 ± 0.03	29.03 ± 1.61	43.15 ± 2.45
		24	0.95 ± 0.03	0.91 ± 0.03	0.92 ± 0.02	56.21 ± 1.68	95.02 ± 2.19
^{177}Lu-Folate-Bombesin	7	1	0.66 ± 0.04	0.61 ± 0.02	0.67 ± 0.04	76.58 ± 2.37	6.55 ± 0.12
		24	0.58 ± 0.01	0.54 ± 0.02	0.56 ± 0.04	14.36 ± 0.96	34.08 ± 2.77
	8	1	0.91 ± 0.01	0.85 ± 0.02	0.91 ± 0.02	81.82 ± 1.21	8.08 ± 0.19
		24	0.84 ± 0.02	0.80 ± 0.01	0.82 ± 0.01	10.06 ± 0.53	40.96 ± 1.50
	9	1	0.19 ± 0.01	0.18 ± 0.01	0.18 ± 0.01	83.37 ± 2.69	8.08 ± 0.19
		24	0.18 ± 0.01	0.17 ± 0.01	0.16 ± 0.01	12.27 ± 0.97	40.96 ± 1.50

ATV1 = pi/6 × W × H × L; ATV2 = 0.5 × W × H × L; CTV = algorithm reconstructed volume; % Volumetric tumor uptake (%VTU); % Volumetric kidney uptake (%VKU)

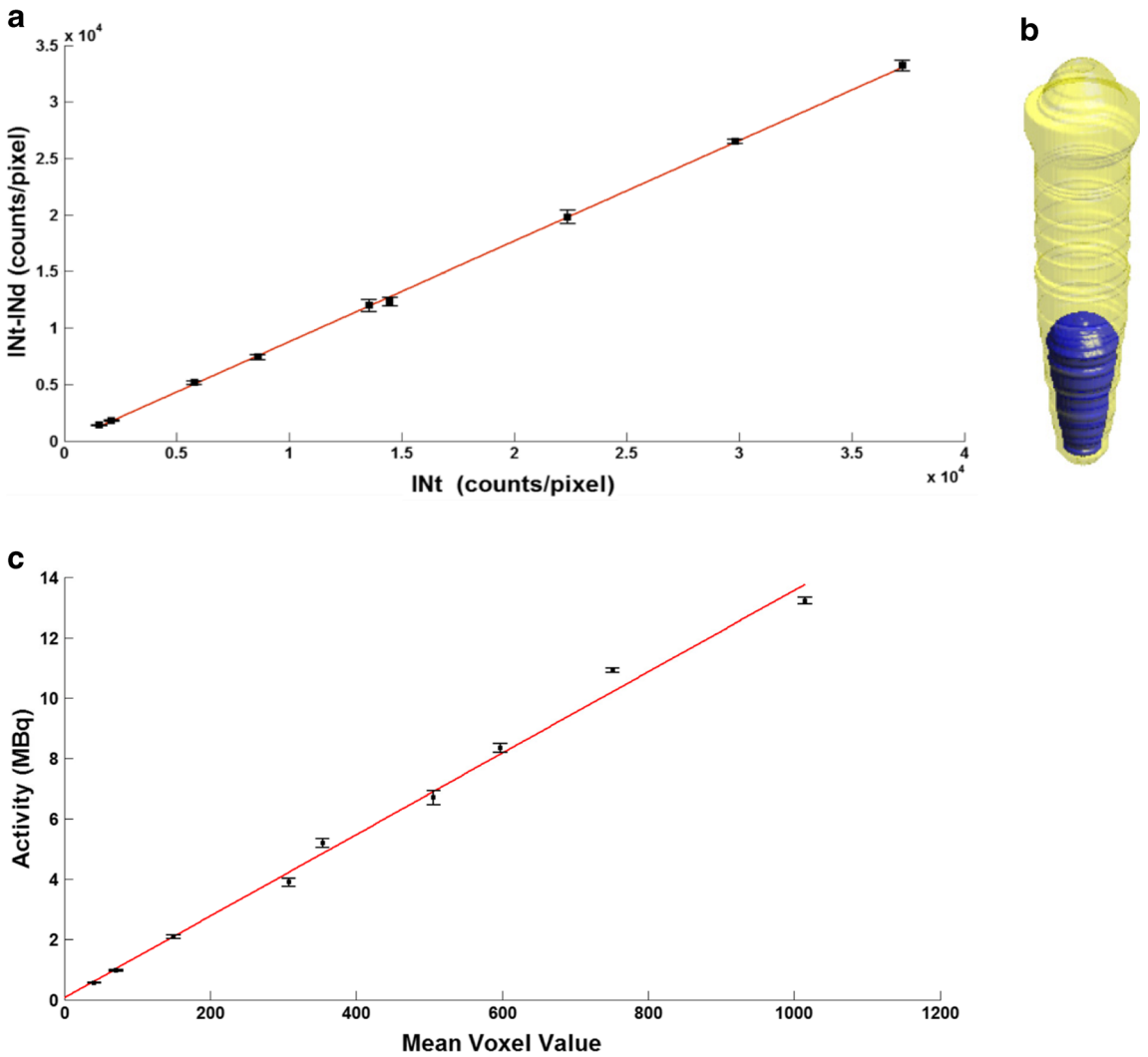

Fig. 10 **a** Graphic representation of (INt − INd) as a function of INt. **b**Tridimensional reconstruction of the tube and the activity. **c** Graphic representation of mean voxel value as a function of activity

3.4 Attenuation factor calculation

The percentage of radiation attenuation due to the mouse body was 29.21 ± 1.53%, calculated from all the images acquired according to the methodology reported. This percentage was used as the attenuation correction factor (AF). The AF was used to correct the intensity of activity quantification in mice images according to the following expression:

$$I_C = \frac{(I_o * 100)}{29.21} = (3.42 * I_o) \tag{5}$$

3.5 Scattering correction factor

Figure 10a depicts the results obtained when the relation [INt vs. (INt-INd)] was analyzed. The same figure demonstrates the linear function regression. This parametric identification analysis yields the following equation:

$$INt - INd = (0.89 * INt) - 123.03 \tag{6}$$

The linear regression analysis produced a correlation coefficient of $R^2 = 0.99$. This equation was used in the activity quantification algorithm to eliminate the counts in the region of interest due to the scattering effect.

3.6 Calibration factor

Figure 10c represents the results obtained for the relationship [mean voxel value vs. activity] as well as its function regression. This linear parametric identification analysis yields a correlation factor of 0.994. The equation that correlates the activity to the mean voxel value is:

$$A(MBq) = (0.0135 * MVV) + 0.0646 \tag{7}$$

Table 2 Biodistribution in mice with T47D-induced tumors after i.v. administration of ^{99m}Tc-Folate-Bombesin, expressed as a percentage of the injected activity per organ (%IA) (mean ± SD, $n = 3$)

Tissue	%IA ± SD		
	0.5 h	2 h	24 h
Tumor	5.69 ± 0.29	4.52 ± 0.23	0.57 ± 0.04
Kidneys	22.23 ± 5.21	17.66 ± 4.14	1.21 ± 0.05

The calibration factor described in Eq. 7 was used to convert the mean voxel value corrected by radiation attenuation and scattering to activity in MBq in the activity quantification algorithm. Table 2 shows the time kinetics of ^{99m}Tc-Folate-Bombesin distribution in both tumor and kidneys. The expected decay of %IA (% of injected activity) in both organic structures was detected. The variation with respect time corresponds to the results observed with similar studies but executed ex vivo.

4 Discussion

The imaging tridimensional reconstruction algorithm developed in this study can be easily extrapolated to different 2D acquisition types of images [46, 47]. Indeed, the same method was applied over three different imaging modalities and no significant differences were detected between the diverse volumetric quantification methods [45]. This characteristic flexibility of the algorithm developed in this study is a remarkable advantage in comparison to similar reconstruction methods [46, 47]. Despite the use of only three biosensors, this do not represent a problem or a limitation due to all the biosensors are based on folate and the biodistribution results would be very similar in each of the imaging modalities which allow a better comparison.

Superimposing of different images is also a novelty of the algorithm proposed here. The image fusion between more than two modalities is a non-standard process in commercial preclinical imaging systems [48, 49]. The method proposed in this study can solve this problem even with the four different modalities included in the BVX system [18]. The capacity of this method helps to confirm the relative anatomic position of the tumor or anatomical regions of interest and its relationship with the functional uptake. Thus, a complementary study can be performed that can improve the final diagnosis and treatment of the tumor.

The simplicity to reproduce the 3D image reconstructions followed the regular tomographic techniques. Thus, image reconstructions developed in this study can be comparable to those attained with some other technological platforms [22, 28, 50]. This adaptability condition is also useful because the superimposition of images can be executed even with images obtained from different equipment but with similar processing algorithms.

Percentages of activity uptake are reproducible and accurate with respect to similar studies executed in similar imaging systems. Moreover, the high correlation degree obtained between the volumetric uptake determined by the reconstruction algorithm and two reference methods of tumor uptake quantification justifies the application of the image-processing methods used in our algorithm [41–43]. This comparison is validated through consideration that the reference methods have been widely used in different validated preclinical studies [51, 52]. It should be noted that these methods require the additional procedure of determining the volume by direct inspection. On the other hand, the method proposed in this study only requires the image reconstruction in two different modalities.

Even when the proposed algorithm in this study was only tested with three different biosensors, the image reconstruction process can be easily extended to a larger set of biosensors whose activity can be detected by any of the modalities included in the BVX system [53–55]. This superior option is a consequence of combining the imaging modalities of BVX and the reconstruction algorithm.

In the same sense, the activity quantification executed by the algorithm can be applied to different radiopharmaceuticals which emit gamma photons [7, 8]. This fact implies a second degree of flexibility that can be highlighted as a remarkable characteristic of the system developed in this study (imaging system and reconstruction algorithm).

5 Conclusions

This study succeeded in developing an integral method to characterize the in vivo volumetric distribution of folate-based biosensors. The effectiveness of the method was confirmed with the accurate detection in mice tumors and kidneys of ^{99m}Tc-Folate-BN, ^{177}Lu-Folate-BN, and FolateRSense™ 680. Evaluation of any biosensor can be improved by using four different imaging techniques: X-ray, radioisotopic, fluorescence, and Cerenkov. A set of image-processing methods (contrast, blurring correction, filtering) enhanced the 3D images, yielding more workable imaging results with compensation of interference by dispersion and attenuation. Image fusion of these results produced a composite that helped in evaluating the biodistribution of all three biosensors. Two standard methods to quantify the volumetric size of the tumors were used as reference. All comparative analysis demonstrated a positive correlation above 0.95. This result justified and validated the method proposed in this study. Several open researching opportunities emerged from the method developed in this study: kinetic modeling of volumetric distribution for different radiopharmaceuticals, and online evaluation of

hybrid (diagnosis-treatment) radiopharmaceutical's effect on tumor distribution and modification of image-processing techniques to improve the quality of the reconstructed image.

Acknowledgements The authors are grateful for the support of the Mexican National Council of Science and Technology (CONACYT-SEP-CB-2014-01-242443 and CONACyT-PDCPN-2015-01-1040) and to the National Polytechnic Institute (IPN-SIPCOFAA-2015-0344). This research was carried out as part of the activities of the "Laboratorio Nacional de Investigación y Desarrollo de Radiofármacos, CONACyT."

Compliance with ethical standards The study was approved by the Institutional Ethical Committee for the Care and Use of Laboratory Animals ("Instituto Nacional de Ciencias Médicas y Nutrición Salvador Zubirán").

References

1. Wang DS, Dake MD, Park JM, Kuo MD (2009) Molecular imaging: a primer for interventionalists and imagers. J Vasc Interv Radiol 20:1405–1423
2. Hoffman RM (2002) In vivo imaging of metastatic cancer with fluorescent proteins. Cell Death Differ 9(8):786–789. https://doi.org/10.1038/sj.cdd.4401077
3. Liu H, Ren G, Miao Z, Zhang X, Tang X, Han P et al (2010) Molecular optical imaging with radioactive probes. PLoS One 5(12):e14484. https://doi.org/10.1371/journal.pone.0014484
4. Stuker F, Ripoll J, Rudin M (2011) Fluorescence molecular tomography: principles and potential for pharmaceutical research. Pharmaceutics 3(4):229–274. https://doi.org/10.3390/pharmaceutics3020229
5. Rao J, Dragulescu-Andrasi A, Yao H (2007) Fluorescence imaging in vivo: recent advances. Curr Opin Biotechnol 18(1):17–25. https://doi.org/10.1016/j.copbio.2007.01.003
6. Ocak M, Gillman AG, Bresee J, Zhang L, Vlad AM, Müller C, Schibli R, Edwards WB, Anderson CJ, Gach HM (2015) Folate receptor-targeted multimodality imaging of ovarian cancer in a novel syngeneic mouse model. Mol Pharm 12(2):542–553. https://doi.org/10.1021/mp500628g
7. Aranda-Lara L, Ferro-Flores G, Ramírez F de M, Ocampo-García B, Santos-Cuevas C, Díaz-Nieto L et al. (2016) Improved radiopharmaceutical based on 99mTc-Bombesin–folate for breast tumour imaging. Nucl Med Commun [Internet]. 37:377–86. Available from: http://content.wkhealth.com/linkback/openurl?sid=WKPTLP:landingpage&an=00006231-201604000-00007
8. Santos-Cuevas CL, Ferro-Flores G, Arteaga de Murphy C, Ramírez FDM, Luna-Gutiérrez MA, Pedraza-López M et al (2009) Design, preparation, in vitro and in vivo evaluation of 99mTc-N2S2-Tat(49-57)-bombesin: a target-specific hybrid radiopharmaceutical. Int J Pharm 375(1-2):75–83. https://doi.org/10.1016/j.ijpharm.2009.04.018
9. Kim SM, Choi N, Hwang S, Yim MS, Lee JS, Lee SM, Cho G, Ryu EK (2013) Folate receptor-specific positron emission tomography imaging with folic acid-conjugated tissue inhibitor of metalloproteinase-2. Bull Kor Chem Soc 34(11):3243–3248. https://doi.org/10.5012/bkcs.2013.34.11.3243
10. Kwekkeboom DJ, Mueller-Brand J, Paganelli G, Anthony LB, Pauwels S, Kvols LK et al (2005) Overview of results of peptide receptor radionuclide therapy with 3 radiolabeled somatostatin analogs. J Nucl Med 46(Suppl 1):62S–66S
11. Chu Z, La Sance K, Blanco V, Kwon C-H, Kaur B, Frederick M et al (2014) In vivo optical imaging of brain tumors and arthritis using fluorescent SapC-DOPS nanovesicles. J Vis Exp [Internet]. 12:1–7. Available from: http://www.jove.com/video/51187/in-vivo-optical-imaging-brain-tumors-arthritis-using-fluorescent-sapc
12. Aranda-Lara L, Ferro-Flores G, Azorin-Vega E, Ramirez FM, Jimenez-Mancilla N, Ocampo-Garcia B et al (2016) Synthesis and evaluation of Lys1(alpha,gamma-Folate)Lys3(177Lu-DOTA)-Bombesin(1–14) as a potential theranostic radiopharmaceutical for breast cancer. Appl Radiat Isot. Elsevier 107:214–219. https://doi.org/10.1016/j.apradiso.2015.10.030
13. Kelemen LE (2006) The role of folate receptor alpha in cancer development, progression and treatment: cause, consequence or innocent bystander? Int J Cancer 119(2):243–250. https://doi.org/10.1002/ijc.21712
14. Teng L, Xie J, Teng L, Lee RJ (2012) Clinical translation of folate receptor-targeted therapeutics. Expert Opin Drug Deliv 9:901–8. Available from: http://www.ncbi.nlm.nih.gov/pubmed/22663189
15. Mitra A, Renukuntla J, Shah S, Boddu SHS, Vadlapudi A, Vadlapatla R, et al (2015) Functional characterization and expression of folate receptor-α in T47D human breast cancer cells. Drug Dev. Ther 6:52. Available from: http://www.ddtjournal.org/text.asp?2015/6/2/52/162441
16. Sancho V, Di Florio A, Moody TW, Jensen RT (2011) Bombesin receptor-mediated imaging and cytotoxicity: review and current status. Curr Drug Deliv 8(1):79–134. https://doi.org/10.2174/156720111793663624
17. Dalm SU, Martens JWM, Sieuwerts a. M, van Deurzen CHM, Koelewijn SJ, de Blois E, et al (2015) In vitro and in vivo application of radiolabeled gastrin-releasing peptide receptor ligands in breast cancer. J Nucl Med 56:752–7. Available from: http://jnm.snmjournals.org/cgi/doi/10.2967/jnumed.114.153023
18. Sasser ATA, Orton SP, Leevy MW (2014) Multimodal in vivo fluorescen, luminescent and X-ray imaging in preclinical studies of inflammation and immunobiology 2009–10
19. Bufkin K, Univversity W, Leevy M, Mentor PD (2015) Multimodal imaging trials with zebrafish specimens. 1:1–5
20. Martí-Bonmatí L, Sopena R, Bartumeus P, Sopena P (2010) Multimodality imaging techniques. Contrast Media Mol Imaging 5:180–9. Available from: http://doi.wiley.com/10.1002/cmmi.393
21. Magota K, Kubo N, Kuge Y, Nishijima K, Zhao S, Tamaki N (2011) Performance characterization of the Inveon preclinical small-animal PET/SPECT/CT system for multimodality imaging. Eur J Nucl Med Mol Imaging 38:742–752. https://doi.org/10.1007/s00259-010-1683-y
22. Hwang JY, Wachsmann-Hogiu S, Ramanujan VK, Ljubimova J, Gross Z, Gray HB et al (2012) A multimode optical imaging system for preclinical applications in vivo: Technology development, multiscale imaging, and chemotherapy assessment. Mol Imaging Biol 14:431–442. https://doi.org/10.1007/s11307-011-0517-z
23. Chapon C, Jackson JS, Aboagye EO, Herlihy AH, Jones WA, Bhakoo KK (2009) An in vivo multimodal imaging study using MRI and PET of stem cell transplantation after myocardial infarction in rats. Mol. Imaging Biol 11:31–38. https://doi.org/10.1007/s11307-008-0174-z
24. Paproski RJ, Li Y, Barber Q, Lewis JD, Campbell RE, Zemp R (2015) Validating tyrosinase homologue melA as a photoacoustic reporter gene for imaging *Escherichia coli*. J Biomed Opt 20:106008. Available from: http://biomedicaloptics.spiedigitallibrary.org/article.aspx?. https://doi.org/10.1117/1.JBO.20.10.106008
25. Doney E, Van Avermaete T, Chapman S, Waldeck J, Leevy WM (2013) Application note # AP0128 Jun 2013 Planar imaging of 99m Tc labeled SPECT probes in living mice using the In-Vivo Xtreme platform with radioisotopic phosphor Screen. 1–5
26. Sumi NJ, Lima E, Pizzonia J, Orton SP, Craveiro V, Joo W, et al (2014) Murine model for non-invasive imaging to detect and monitor ovarian cancer recurrence. J. Vis. Exp. [Internet]. e51815.

Available from: http://www.jove.com/video/51815/murine-model-for-non-invasive-imaging-to-detect-monitor-ovarian
27. Hu GHG, Li HLH, Yao JYJ, Bai JBJ (2008) Fluorescent optical imaging of small animals using filtered back-projection 3D surface reconstruction method. 2008 Int Conf Biomed Eng Informatics 2: 1000–1004
28. Kuo C, Coquoz O, Troy TL, Xu H, Rice BW (2007) Three-dimensional reconstruction of in vivo bioluminescent sources based on multispectral imaging. J Biomed Opt 12(2):024007. https://doi.org/10.1117/1.2717898
29. Song JS, Lee JM, Sohn JY, Yoon J-H, Han JK, Choi BI (2015) Hybrid iterative reconstruction technique for liver CT scans for image noise reduction and image quality improvement: evaluation of the optimal iterative reconstruction strengths. Radiol. Med 120: 259–267. https://doi.org/10.1007/s11547-014-0441-9
30. Koch W, Suessmair C, Tatsch K, Pöpperl G (2011) Iterative reconstruction or filtered backprojection for semi-quantitative assessment of dopamine D2 receptor SPECT studies? Eur. J. Nucl. Med. Mol. Imaging 38:1095–1103. https://doi.org/10.1007/s00259-011-1737-9
31. Zeng GL (2010) Medical image reconstruction: a conceptual tutorial. Springer Berlin Heidelberg, Berlin, Heidelberg, pp 125–173. https://doi.org/10.1007/978-3-642-05368-9_6
32. Kikuchi S, Matsuya A, Yamaguchi M, Ohyama N (1996) Microscopic computed tomography based on generalized analytic reconstruction from discrete samples. Opt Rev 3:22–28. https://doi.org/10.1007/s10043-996-0022-9
33. Aguirre J, Sisniega A, Ripoll J, Desco M, Vaquero JJ (2008) Design and development of a co-planar fluorescence and X-ray tomograph. IEEE Nucl Sci Symp Conf Rec 5412–3
34. Ducros N, Bassi A, Valentini G, Canti G, Arridge S, D'Andrea C (2013) Fluorescence molecular tomography of an animal model using structured light rotating view acquisition. J Biomed Opt 18(2):020503. https://doi.org/10.1117/1.JBO.18.2.020503
35. Liu X, Wang D, Bai J (2009) Fluorescence molecular tomography with optimal radon transform based surface reconstruction. Conf Proc IEEE Eng Med Biol Soc 2009:1404–1407. https://doi.org/10.1109/IEMBS.2009.5334178
36. Butz T. Fourier transformation for pedestrians. Cham: Springer International Publishing; 2015. p. 173–81. Available from: https://doi.org/10.1007/978-3-319-16985-9_7
37. Jähne B (1995) Digital image processing: concepts, algorithms, and scientific applications. Springer Berlin Heidelberg, Berlin, Heidelberg, pp 231–252. https://doi.org/10.1007/978-3-662-03174-2_13
38. Prabhat P, Arumugam S, Madan VK (2012) Filtering in filtered backprojection computerized tomography. Proc NCNTE-2012 4–7
39. Kendziorra C, Meyer H, Dewey M (2015) Implementation of a phase detection algorithm for dynamic cardiac computed tomography analysis based on time dependent contrast agent distribution. PLoS one [internet]. Public Libr Sci 9:1–12. https://doi.org/10.1371/2Fjournal.pone.0116103
40. Hautière N, Tarel J-P, Aubert D, Dumont É (2008) Blind Contrast enhancement assessment by gradient ratioing at visible edges. Image Anal. Stereol. [Internet]. 27:87–95. Available from: http://www.ias-iss.org/ojs/IAS/article/view/834
41. Valencia-Murillo JF (2014) Poveda-Sendales DA, Valencia-Vargas DF. Evaluating the impact of image preprocessing on iris segmentation. Tecno Lógicas 17:31–41
42. Polesel A, Ramponi G, Mathews VJ (2000) Image enhancement via adaptive unsharp masking. IEEE Trans Image Process 9(3):505–510. https://doi.org/10.1109/83.826787
43. Ogoda M, Hishinuma K, Yamada M, Shimura K (1997) Unsharp masking technique using multiresolution analysis for computed radiography image enhancement. J Digit Imaging [Internet]. 10:185–9. Available from: http://www.pubmedcentral.nih.gov/articlerender.fcgi?artid=3452800&tool=pmcentrez&rendertype=abstract
44. Suter SK, Ma B, Entezari A (2014) Advances in visual computing: 10th International Symposium, ISVC 2014, Las Vegas, NV, USA, December 8–10, 2014, Proceedings, Part I. In: Bebis G, Boyle R, Parvin B, Koracin D, McMahan R, Jerald J, et al., editors. Cham: Springer International Publishing. p. 313–22. Available from: https://doi.org/10.1007/978-3-319-14249-4_30
45. Tomayko MM, Reynolds CP (1989) Determination of subcutaneous tumor size in athymic (nude) mice. Cancer Chemother. Pharmacol 24:148–154. https://doi.org/10.1007/BF00300234
46. Schumann S, Liu L, Tannast M, Bergmann M, Nolte L-P, Zheng G (2013) An integrated system for 3D hip joint reconstruction from 2D X-rays: a preliminary validation study. Ann Biomed Eng 41: 2077–2087. https://doi.org/10.1007/s10439-013-0822-6
47. Arranz A, Rudin M, Zaragoza C, Ripoll J (2015) Methods in mouse atherosclerosis. In: Andrés V, Dorado B, editors. New York, NY: Springer New York. p. 367–76. Available from: https://doi.org/10.1007/978-1-4939-2929-0_27
48. Backfrieder W, Hanel R, Diemling M, Lorang T, Kettenbach J, Imhof H (2001) Digital (R) evolution in radiology. In: Hruby W, editor. Vienna: Springer Vienna p. 131–9. Available from: https://doi.org/10.1007/978-3-7091-3707-9_16
49. Asaithambi N, Kayalvizhi R, Selvi W. Proceedings of the International Conference on Soft Computing Systems: ICSCS 2015, Volume 1. In: Suresh PL, Panigrahi KB, editors. New Delhi: Springer India; 2016. p. 415–25. Available from: https://doi.org/10.1007/978-81-322-2671-0_40
50. Chin PTK, Welling MM, Meskers SCJ, Valdes Olmos RA, Tanke H, Van Leeuwen FWB (2013) Optical imaging as an expansion of nuclear medicine: Cerenkov-based luminescence vs fluorescence-based luminescence. Eur J Nucl Med Mol Imaging 40(8):1283–1291. https://doi.org/10.1007/s00259-013-2408-9
51. Lee YC, Fullerton GD, Goins BA (2015) Comparison of multimodality image-based volumes in preclinical tumor models using *In-Air* micro-CT image volume as reference tumor volume. Open J. Med. Imaging [Internet]. 05:117–32. Available from: http://www.scirp.org/journal/PaperInformation.aspx?PaperID=59462&#abstract
52. van Driel PB a. a., van de Giessen M, Boonstra MC, Snoeks TJ a., Keereweer S, Oliveira S, et al. (2014) Characterization and evaluation of the artemis camera for fluorescence-guided cancer surgery. Mol. Imaging Biol. [Internet]. 17:413–23. Available from: http://link.springer.com/10.1007/s11307-014-0799-z
53. Ferro-flores G, Ocampo-garcía BE, Santos-cuevas CL, María F De, Azorín-vega EP, Meléndez-alafort L (2015) Theranostic radiopharmaceuticals based on gold nanoparticles labeled with 177 Lu and conjugated to peptides 150–9
54. Jiménez-Mancilla N, Ferro-Flores G, Santos-Cuevas C, Ocampo-García B, Luna-Gutiérrez M, Azorín-Vega E, et al (2013) Multifunctional targeted therapy system based on (99m) Tc/(177) Lu-labeled gold nanoparticles-Tat(49–57)-Lys(3)-bombesin internalized in nuclei of prostate cancer cells. J. Labelled Comp. Radiopharm. [Internet]. 56:663–71. Available from: http://www.ncbi.nlm.nih.gov/pubmed/25196028
55. Shrivastava A, Ding H, Kothandaraman S, Wang S-H, Gong L, Williams M et al (2014) A high-affinity near-infrared fluorescent probe to target bombesin receptors. Mol Imaging Biol 16:661–669. https://doi.org/10.1007/s11307-014-0727-2

Gerardo Julián Ramírez-Nava . Bachelor in Biomedical Engineering at National Polytechnic Institute (Mexico City); student of the Master in Medical Physics at Autonomous University of the State of Mexico.

Isaac Chairez , PhD. in Automatic Control. Researcher at the Professional Interdisciplinary Unit of Biotechnology, México. His research focuses in neural networks, fuzzy control theory, nonlinear control, and adaptive control.

Clara Leticia Santos-Cuevas , PhD. in Medical Physics. Researcher at Radiopharmaceutical Development of National Institute of Nuclear Research, Mexico, and has been dedicated to molecular imaging in nuclear medicine.

Liliana Aranda-Lara . Bachelor in Biology; M. Sc. specialized in Health Physics and PhD. student in Health Sciences at Autonomous University of the State of Mexico.